

A hybrid Vlasov method for nonlinear wave-particle interaction in weakly inhomogeneous magnetic field

Jiangshan Zheng^a, Bo Li^a, Ge Wang^b

^aSchool of Physics, Beihang University, Beijing, Beijing 100191, China

^bInstitute for Fusion Studies, The University of Texas, Austin, Texas, 78712, USA

Abstract

We present a hybrid Lagrangian-Eulerian Vlasov solver for nonlinear resonant wave-particle interactions problems in weakly inhomogeneous magnetic field. The governing Vlasov equation is derived from a recently proposed resonance tracking Hamiltonian method. The method tracks the dynamics of deeply trapped resonant particles in a narrow-banded coherent wave. It gives the evolution of the distribution function with a scale separated Hamiltonian that containing the slowly-varying motion about the resonant frame of reference and fast-varying coherent interactions. The hybrid method solves the slowly-varying phase space dynamics by Lagrangian method along the resonant trajectory, while manages the fast-varying phase-space evolution in Eulerian grid with an adaptive time step interpolated differential operator scheme. We apply our method to study the frequency chirping problem of whistler mode chorus wave in the Earth magnetosphere and successfully reproduce the chirping chorus wave. The results are in well agree with previous studies. Aiming at the nonlinear resonant wave-particle interaction in the weakly inhomogeneous regime, our approach can give high resolution for the fast varying phase space at low computational cost. It could provide additional insights of the wave instabilities and particle energy transfer compared to the conventional Vlasov and particle-in-cell methods.

1. Introduction

Wave-particle interaction, especially the nonlinear resonant one is of great importance and have been extensively discussed in a broad spectrum of plasma physics. In magnetically confined fusion devices, there have Alfvén wave instabilities [1, 2] which are associated with mode frequency sweeping and lead to premature ejection of alpha particles that deteriorate plasma confinement [3]. In the planetary magnetosphere [4], as well as in the laboratory devices [5, 6], people have studied the chorus wave, which is associated with various geophysical activity like relativistic electron precipitation, X-ray microbursts, pulsating and diffuse auroras [7, 8, 9]. It has been demonstrated that the nonlinear resonant interaction between toroidal Alfvén eigenmodes and fusion-born alpha particles, the energetic electrons and the whistler-mode wave play the key role in such nonlinear instabilities, and therefore it is greatly concerned to build solid and various theoretical descriptions and numerical models to further discuss those wave-particle interactions.

In general, the wave-particle interactions can be described by the Vlasov equation and self-consistently coupled with the wave evolution. In the homogeneous plasmas [10, 11] or in the nonuniform regime with spatial symmetry [12, 13, 14], the involved wave can be treated as standing wave with stationary fixed wavenumber or mode number, and the interactions are localized without any spatial dependence. Thus the simulation is relatively straightforward due to the system’s inherent periodicity. It only needs to consider the momentum space in one local spatial volume, which is essentially a single scale wave-particle interaction problem and farvorable to solve numerically.

However, when dealing with inhomogeneous cases where the periodicity falls short, things becomes complicated. The nonuniform spatial dependence brings extra dimensions on both the wave evolution and the fine structures of resonance particle phase space. The interaction have to be considered on the whole domain instead of in a single spatial volume. Although, techniques like WKB approximation [15] or slowly varying envelope approximation [16] can be applied to simplify the wave calculation, it is hard to find a suitable approach to split the scales of the resonant particles due to intricate wave-particle interactions along the inhomogeneous magnetic field. Therefore, the fast varying varying temporspatial scales are involved in all dimensions of the resonant particle phase space which brings tremendous workload than that in the homogeneous plasma settings. Also, it becomes clear that traditional methods lack the required precision to describe the nuanced behavior of particles subjected to the nonlinearity imposed by inhomogeneous magnetic fields and chirping waves.

To address these shortcomings, we have proposed a novel theoretical framework [] that describes the physics on the reference frames moving in the local resonant velocity. We transcend the stationary phase approximation [17, 18], and expand the wave phase about the local resonance center which naturely decouples the motion scales. We compose a new Hamiltonian represented in the new canonical coordinates and momentum. The Hamiltonian can be splitted into two subspaces, the one is ξ, Ω corresponding to the fast-varying wave particle interaction terms, and the other is ϑ, \mathcal{J} corresponding to the slowly-varying one seen by the resonance frame moving along the resonance trajectory. Thus, the fast varying scales in the whole dimensions are now reduced by half, and the fast-varying wave

particle interactions phase space ξ, Ω can be studied with a relaxed resolution in ϑ, \mathcal{J} domain than that in the origin laboratory frame. The particle slowly varying scale corresponds to the characteristic length of background plasma inhomogeneity, and the dynamics in ξ, Ω subspace can be treated as quasi-periodical in ξ dimension, same as that in the homogeneous plasma. Base on previous analysis, we write the corresponding Vlasov equation for the resonance particles distribution function $f(t, s_i, \vartheta, \mathcal{J}, \xi, \Omega)$. The equation is readily constructed as advective form of two separated Hamiltonian flows and the advective term of reframe moving along resonance trajectories.

$$\frac{\partial f}{\partial t} + \frac{ds_i}{dt} \frac{\partial f}{\partial s_i} + [f, H]_{\vartheta, \mathcal{J}} + [f, H]_{\xi, \Omega} = 0, \quad (1)$$

where the bracket is the canonical Poisson bracket.

The Vlasov equation consists of two separated motions that can be naturally solved by hybrid method individually. Here we develop a delta f Vlasov solver based on an elaborated hybrid Lagrangian-Eulerian method for solving such system [19] for such general form. A conservative form Interpolated Differential Operator (IDO-CF) method is applied to the Eulerian grid solve the evolution in ξ, Ω domain, it provide a high resolution for recognizing the formation and evolution of resonant structures due to the fast varying wave-particle interaction. On the other hand, the Lagrangian markers as a sampling points in ϑ, \mathcal{J} domain on each resonance frame center s_i are applied to track the slowly varying dynamics. In addition, an adaptive time step RK solver is applied to the Eulerian part to link the gap between the time step of the two subspaces.

As to the wave evolution, we focus on the slowly varying envelope of the wave in the resonance frame. From the Ampere's law, we can obtain various form of wave equation regarding the wave envelope. Here, we use a 1D whistler wave frequency chirping problem in the Earth magnetosphere as an example. The results show good agreement linear predictions, other nonlinear simulations and satellite observations. By incorporating advanced numerical techniques and a more comprehensive understanding of the magnetic field variations, we endeavor to uncover the elusive fine structure of resonant particles. This endeavor holds the potential to revolutionize our comprehension of the intricate interplay between waves and particles within inhomogeneous magnetic fields.

We organized our paper as follows. In section 2, we present the HLE theory for our scale separated Vlasov system and introduce the IDO-CF numerical scheme. In section 3, we present the details of the numerical modeling on the wave slowly varying envelope. Section 4 provides a detailed description on our code design and implementations. Finally, the conclusion is provided in section 6.

Before introducing our numerical scheme, we first show the normalization for the equations. The original equations in our previous studies are written in Gaussian unit. Here we use electron mass m_e , electron charge e , speed of light c and background electron plasma frequency ω_{pe} to normalize mass, charge, velocity and time. Other units for quantities like \mathcal{J} and vector potential A can be derived from the related governing equations as:

$$[A] : \frac{m_e c^2}{e}, \quad [J] : \frac{m_e c^2}{\omega_{pe}}. \quad (2)$$

The physical constants are now eliminated in the normalized equations.

2. The Hybrid Lagrangian Eulerian Solver for the Vlasov system

Consider the delta f form of Vlasov system in equation (1). The evolution of perturbed distribution function $\delta f(s_i, \vartheta, \mathcal{J}, \xi, \Omega)$ is

$$\frac{\partial \delta f}{\partial t} + \frac{ds_i}{dt} \frac{\partial \delta f}{\partial s_i} + [\delta f, H]_{\vartheta, \mathcal{J}} + [\delta f, H]_{\xi, \Omega} = \mathcal{S}, \quad (3)$$

where the Poisson brackets are defined as

$$[f, g]_{x,y} = \frac{\partial f}{\partial x} \frac{\partial g}{\partial y} - \frac{\partial f}{\partial y} \frac{\partial g}{\partial x}. \quad (4)$$

Here ξ, Ω and ϑ, \mathcal{J} are the canonical variables corresponding to the fast and slowly varying scales, respectively. The source term $\mathcal{S} = -[f_0, \delta H]_{\vartheta, \mathcal{J}} - [f_0, \delta H]_{\xi, \Omega}$ where f_0 is the equilibrium distribution function and δH denotes the perturbed Hamiltonian due to the resonant wave-particle interactions. Note that the derivatives of δH with respect to the slowly varying coordinates ϑ and \mathcal{J} can be neglected due to the separation of perturbation and equilibrium scales and $\partial f_0 / \partial \xi = 0$ since the equilibrium distribution function does not generally depend on the fast varying angle coordinate ξ . Thus the source term can be simplified as

$$\mathcal{S} = \frac{\partial \delta H}{\partial \xi} \frac{\partial f_0}{\partial \Omega}. \quad (5)$$

We now apply the HLE method to the Vlasov system where the fast and slowly varying scales have been separated in the Hamiltonian theory. We model the fast varying phase space ξ, Ω by Eulerian method and model the slowly varying dimensions ϑ, \mathcal{J} and resonance frame coordinate s_i thorough Lagrangian method. The distribution function is written as [19]

$$\delta f(\vartheta, \mathcal{J}, \xi, \Omega; s_i, t) = \sum_i \mathcal{F}_i(t, \xi, \Omega) \delta(s - s_i, \vartheta - \vartheta_i, \mathcal{J} - \mathcal{J}_i), \quad (6)$$

where $\mathcal{F}_i(t, \xi, \Omega)$ is the distribution function in ξ, Ω space, and the delta function represents the markers on Lagrangian space s_i, ϑ_i , and \mathcal{J}_i with i the index of the marker. Then the evolution equation for $\mathcal{F}_i(t, \xi, \Omega)$ is [19]

$$\frac{\partial \mathcal{F}_i}{\partial t} + [\mathcal{F}_i, H]_{\xi, \Omega} = \mathcal{S}. \quad (7)$$

For the Lagrangian step, the movement of the maker on spatial domain is given by

$$\dot{s}_i = v_r(s_i, t), \quad (8)$$

where v_r is the resonant velocity. The motion equations for ϑ, \mathcal{J} are [19]

$$\begin{aligned} \dot{\vartheta} &= \frac{\iint \mathcal{F}_i(t, \xi, \Omega) [\vartheta, H]_{\vartheta, \mathcal{J}} d\xi d\Omega}{\iint \mathcal{F}_i(t, \xi, \Omega) d\xi d\Omega}, \\ \dot{\mathcal{J}} &= \frac{\iint \mathcal{F}_i(t, \xi, \Omega) [\mathcal{J}, H]_{\vartheta, \mathcal{J}} d\xi d\Omega}{\iint \mathcal{F}_i(t, \xi, \Omega) d\xi d\Omega}. \end{aligned} \quad (9)$$

Note that, follows our Hamiltonian theory [], the variation of ϑ coordinate is proportional to the background inhomogeneity. Thus, for the weakly inhomogeneous case the variation of the angle coordinate ϑ is considerably small. Besides, the dynamics of J , Ω and ξ are also independent on ϑ , i.e., the system is ϑ -free, and we can neglect the evolution of ϑ . Moreover, the dynamics of momentum \mathcal{J} is fully decoupled with ξ , Ω dimension, thus the integration over the fast varying dimension can be eliminated, and the force equations in our simulation scheme are

$$\begin{aligned}\dot{\vartheta} &\ll 1, \\ \dot{\mathcal{J}} &= [\mathcal{J}, H]_{\vartheta, \mathcal{J}} .\end{aligned}\tag{10}$$

2.1. The Eulerian step

For the numerical treatment, the Vlasov equation (7) is expressed as

$$\frac{\partial g}{\partial t} + m \frac{\partial g}{\partial \xi} - n \frac{\partial g}{\partial \Omega} = \mathcal{S} ,\tag{11}$$

where $g \equiv \mathcal{F}_i$ and

$$m(\xi, \Omega) = \frac{\partial H}{\partial \Omega}, \quad n(\xi, \Omega) = \frac{\partial H}{\partial \xi} .\tag{12}$$

To achieve high-order accuracy we apply the Interpolated Differential Operator (IDO) method [20] to solve the 2D Vlasov equation in ξ, Ω domain. The IDO scheme applies the polynomial as local interpolation functions to replace the distributions along each coordinate in phase space. Here a second-order polynomial is used as interpolation stencil for a function $g(x)$ from x_i to x_{i+1} ,

$$G(x, g_i, g_{i+1}, \sigma_{i+\frac{1}{2}}) = a(x - x_i)^2 + b(x - x_i) + c ,\tag{13}$$

where $g_i \equiv g(x_i)$, $g_{i+1} \equiv g(x_{i+1})$ are function values on the grid, and $\sigma_{i+\frac{1}{2}}$ is the cell integral value

$$\sigma_{i+\frac{1}{2}} \equiv \int_{x_i}^{x_{i+1}} g(x) \, dx ,\tag{14}$$

and the coefficients are determined and from the grid value and the line integral over the cell,

$$\begin{aligned}a &= \frac{3(g_i + g_{i+1})}{\Delta x^2} - \frac{6\sigma_{i+\frac{1}{2}}}{\Delta x^3} , \\ b &= -\frac{2(2g_i + g_{i+1})}{\Delta x} + \frac{6\sigma_{i+\frac{1}{2}}}{\Delta x^2} , \\ c &= g_i .\end{aligned}\tag{15}$$

To demonstrate the IDO-scheme applied in our numerical scheme, we write the discretized form of the Vlasov equation (7),

$$g_{t;i,j} = -m_{i,j} g_{\xi;i,j} - n_{i,j} g_{\Omega;i,j} + \mathcal{S}_{i,j} ,\tag{16}$$

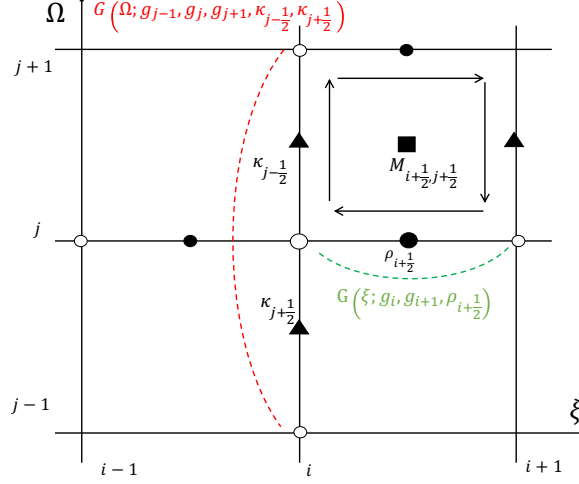


Figure 1: The interpolating functions and cell integrated values in ξ, Ω domain.

where i and j are the grid index for ξ and Ω , g_ξ and g_Ω denote the derivatives along ξ and Ω directions, respectively. The grid and the sampling points are demonstrated in Fig. 1. Applying the interpolation function G defined in Eq. (13) along ξ and Ω yields the derivatives

$$\begin{aligned} g_{\xi; i, j} &\simeq \left. \frac{\partial}{\partial \xi} G(\xi; g_{i, j}, g_{i+1, j}, \rho_{i+\frac{1}{2}, j}) \right|_{i, j}, \\ g_{\Omega; i, j} &\simeq \left. \frac{\partial}{\partial \Omega} G(\Omega; g_{i, j}, g_{i, j+1}, \kappa_{i, j+\frac{1}{2}}) \right|_{i, j}, \end{aligned} \quad (17)$$

where the line integrated values $\rho_{i+\frac{1}{2}, j} = \int_{\xi_i}^{\xi_{i+1}} g_{i, j} d\xi$ and $\kappa_{i, j+\frac{1}{2}} = \int_{\Omega_j}^{\Omega_{j+1}} g_{i, j} d\Omega$. Integrating Eq. (16) along ξ and Ω over the grid interval yields the time evolution of the integral values

$$\begin{aligned} \rho_{i+\frac{1}{2}, j} &= \int_{\xi_i}^{\xi_{i+1}} [-m_j(\xi) g_{\xi; j}(\xi) - n_j(\xi) g_{\Omega; j}(\xi) + S_j(\xi)] d\xi \\ \kappa_{i, j+\frac{1}{2}} &= \int_{\Omega_j}^{\Omega_{j+1}} [-m_i(\Omega) g_{\xi; i}(\Omega) - n_i(\Omega) g_{\Omega; i}(\Omega) + S_i(\Omega)] d\Omega \end{aligned} \quad (18)$$

We apply the third-order central interpolation scheme to approximate the functions m and n along the ξ and Ω dimension and use the interpolating stencil to approximate the derivatives,

$$\begin{aligned} g_{\xi; j}(\xi) &\simeq G(\xi; g_{\xi; i, j}, g_{\xi; i+1, j}, g_{i+1, j} - g_{i, j}) \\ g_{\Omega; j}(\xi) &\simeq G(\xi; g_{\Omega; i, j}, g_{\Omega; i+1, j}, \rho_{\Omega; i+\frac{1}{2}, j}) \\ g_{\Omega; i}(\Omega) &\simeq G(\Omega; g_{\Omega; i, j}, g_{\Omega; i, j+1}, g_{i, j+1} - g_{i, j}) \\ g_{\xi; i}(\Omega) &\simeq G(\Omega; g_{\xi; i, j}, g_{\xi; i, j+1}, \kappa_{\xi; i, j+\frac{1}{2}}) \end{aligned} \quad (19)$$

We apply additional interpolation functions to approximate the derivatives

$$\begin{aligned}\rho_{\Omega; i+\frac{1}{2}, j} &\simeq \frac{\partial}{\partial \Omega} G(\Omega; \rho_{i+\frac{1}{2}, j}, \rho_{i+\frac{1}{2}, j+1}, M_{i+\frac{1}{2}, j+\frac{1}{2}}) \Big|_{i+\frac{1}{2}, j}, \\ \kappa_{\xi; i, j+\frac{1}{2}} &\simeq \frac{\partial}{\partial \xi} G(\xi; \kappa_{i, j+\frac{1}{2}}, \kappa_{i+1, j+\frac{1}{2}}, M_{i+\frac{1}{2}, j+\frac{1}{2}}) \Big|_{i, j+\frac{1}{2}},\end{aligned}\quad (20)$$

where the surface integral $M_{i+\frac{1}{2}, j+\frac{1}{2}} = \int_{\xi_i}^{\xi_{i+1}} \int_{\Omega_j}^{\Omega_{j+1}} g_{i,j} d\xi d\Omega$. The time evolution of this surface integral is given by

$$\begin{aligned}M_{t; i+\frac{1}{2}, j+\frac{1}{2}} &= \int_{\xi_i}^{\xi_{i+1}} n_{j+1}(\xi) g_{j+1}(\xi) d\xi - \int_{\Omega_j}^{\Omega_{j+1}} m_{i+1}(\Omega) g_{i+1}(\Omega) d\Omega \\ &\quad - \int_{\xi_i}^{\xi_{i+1}} n_j(\xi) g_j(\xi) d\xi + \int_{\Omega_j}^{\Omega_{j+1}} m_i(\Omega) g_i(\Omega) d\Omega \\ &\quad + \iint \mathcal{S} d\xi d\Omega.\end{aligned}\quad (21)$$

Here the integral of the source term is solved by trapezoidal integration.

The equations (16), (18), and (21) are a set of ordinary differential equations that can be solved by Runge-Kutta (RK) method. For the boundary conditions, the distribution function in the resonant frame is assumed to be periodic in the phase angle ξ ,

$$g(\xi, \Omega, t) = g(\xi + 2\pi, \Omega, t) \quad (22)$$

and the value of the perturbed distribution vanishes at the Ω boundaries.

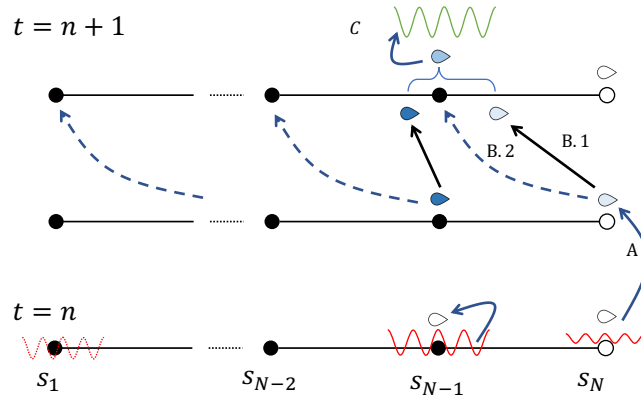


Figure 2: Schematic illustration of the hybrid Vlasov simulation scheme.

2.2. The Lagrangian step

For the Lagrangian markers, without the calculation for ϑ , we sample the markers at s and \mathcal{J} dimension. We use N_s points for sampling s , which is equal to the number of the grids used to discretize the wave equation. We use $N_{\mathcal{J}}$ sampling points in \mathcal{J} dimension for each s_i . Thus the total number of the Lagrangian markers is $N_{\mathcal{J}} \times N_s$. On the s dimension, the markers are initially set one to one onto the fixed wave grids. The sampling point for \mathcal{J} is chosen to ensure a uniform sampling to the initial equilibrium distribution function $f(\mathcal{J})$ at a given s , i.e.,

$$f(J_j) = j/N_{\mathcal{J}}, \quad j = 1, N_{\mathcal{J}}, \quad (23)$$

Since the velocity for each maker is different, to persist the spatial alignment between Lagrangian markers and the fixed grid, we apply a nonuniform grid i.e., an initial nonuniform sampling points. To arrange the initial nonuniform sampling and grids, we first calculate the transit time of a maker through the whole simulation domain consists of N grids, entering from boundary s_1 , going to

$$T = \int_{s_1}^{s_N} \frac{ds}{v_r^l(s)}. \quad (24)$$

s_1 and s_N denote the two end points of the domain, $v_r^l(s)$ is the local resonant velocity that has been predetermined from background equilibrium parameter. Then the simulation time step is set as $\Delta t = T/N$. The grids are set according to

$$s_i = s_{i-1} + v_r^l(s(t))\Delta t. \quad (25)$$

An illustration of the nonuniform is shown in Fig. 3. Now, with such nonuniform grid, the initially sampled Lagrangian markers on grid reached the next adjacent grid as time iterates.

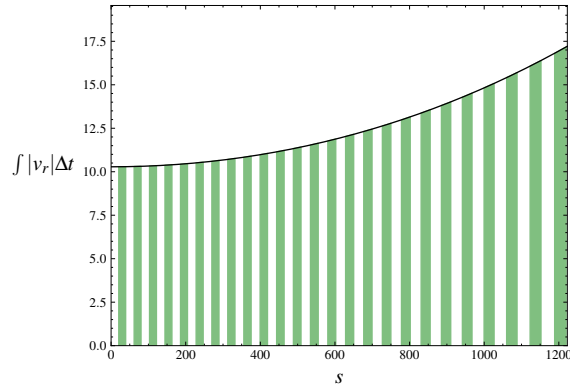


Figure 3: The nonuniform spatial grid obtained from resonance velocity.

The trajectory for each Lagrangian marker s_i, \mathcal{J}_j is determined by equations (8) and (10). We only need to successively push s_i to next grid, drop the maker which leaves the simulation zone, and set new distribution $g(\xi, \Omega) = 0$ for which enters the simulation domain

at each time iteration. \mathcal{J}_j can be integrated by the Runge-Kutta (RK) method from the initial sampling points.

After push the Lagrangian maker from n^{th} to $n+1^{\text{th}}$ step, the distribution $g(t^{n+1}, \xi, \Omega)$ from the Eulerian iteration is moved to this new localtion $s_i^{n+1}, \mathcal{J}_j^{n+1}$. The equillbrium quantities are recalculate at $s_i^{n+1}, \mathcal{J} + n + 1_j$ and used to evolve the next iteration of the distribution at $\xi - \Omega$ space.

Besides, we also apply the uniform wave grid and corresponding sampling of Lagrangian marker on s for the verification of nonuniform grid approach. After a given time step Δt the markers deviated from the fixed grid, thus we need to interpolate the distribution fucntion and its derivatives required in the IDO scheme from adjacent marker to the fixed s grid. The procedures are simliar to the semi-Lagrangian method [21, 22]. After interpolation, the markers realigned to the grid, and the next iteration start again from the grid location. As shown in Fig. 4, the wave amplitudes calculated from the two approaches converge as the smaller grid sizes are used for the uniform grid with interpolation. The evolution of ϑ, \mathcal{J} in

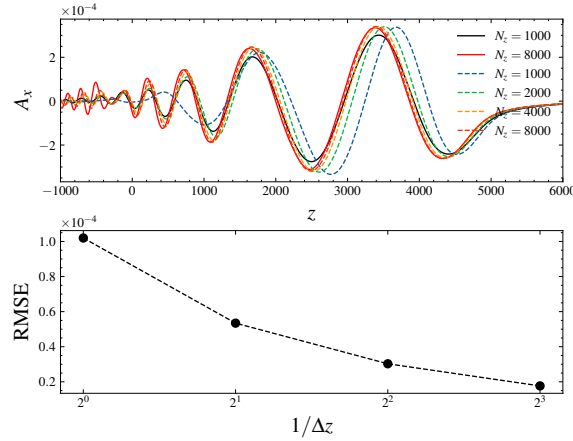


Figure 4: Wave amplitude from semi-Lagrangian method with linear interpolation of distribution at different uniform grid sizes (dashed-line) and the nonuniform grid (solid line).

Eq. (10) are simply solved by applying the RK method.

Since the evolution in ξ, Ω phase space is much faster than that in the $s_i, \vartheta, \mathcal{J}$ domain, we use the large fixed time step Δt for the Lagrangian calculation and apply a much smaller time step Δt_{adp} for solving the fast varying dynamics on the Eulerian domain. Here the smaller time steps Δt_{adp} are adaptively obtained from real time error analysis using the adaptive time step RK method. Thus

$$\sum_{n=1}^N \Delta t_{adp} = \Delta t . \quad (26)$$

where N is the total number of iterations within one Δt . As shown in Fig. 5, Δt_{adp} is adjusted and reduced to a smaller value to satisfy the error constraint. As the system evolves nonlinearly, the time step Δt_{adp} is also refined and the iterations automatically increase within one Δt . It is clearly that the adaptive hybrid methods greatly enhance the computation efficiency.

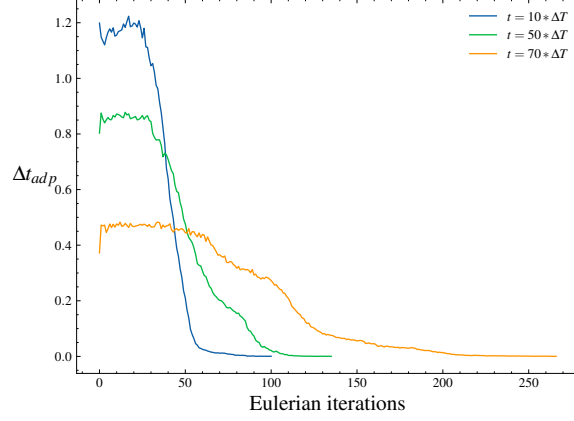


Figure 5: The variation of time step Δt_{adp} with the number of iterations for Eulerian calculation.

3. Wave Equation

We now couple the HLE Vlasov solver with the wave equation to self-consistently study the resonant wave-particle interactions. Here we consider the interaction between energetic electrons and chorus waves in the magnetosphere. The chorus is a circularly polarized electromagnetic wave propagating along the Earth's dipole magnetic field. The vector potential $\mathbf{A}(s, t)$ for the transverse wave is written as

$$\mathbf{A}(s, t) = \mathbf{a}(s, t)e^{i\phi_f}, \quad (27)$$

where ϕ_f is the fast varying phase and $\mathbf{a}(s, t)$ is the slowly varying envelope of the wave packet. The second order wave equation for the chorus in the resonant frame is

$$\begin{aligned} \frac{\partial^2 a}{\partial t^2} - \frac{\partial^2 a}{\partial s_i^2} + 2i\omega_l \frac{\partial a}{\partial t} + 2ik_l \frac{\partial a}{\partial s_i} + \\ \frac{\omega_p^2 \omega_{ce}}{(\omega_{ce} - \omega_l)} \int_0^t d\tau \frac{\partial a}{\partial \tau} e^{-i(\omega_l - \omega_{ce})(t - \tau)} = 4\pi j_p, \end{aligned} \quad (28)$$

where $a = a_x + ia_y$ with x and y the directions perpendicular to the magnetic field. The plasma current consists of the currents from cold electrons and energetic electrons and the cold electron current can be analytically integrated. We write the second-order wave equation (28) in the normalized form as

$$\begin{aligned} \frac{dy_0}{dt} &= y_1 \\ \frac{dy_1}{dt} &= -2i\omega_l y_1 + \frac{\partial^2 y_0}{\partial s^2} - 2ik_l \frac{\partial y_0}{\partial s} - \frac{\omega_p^2 \omega_{ce}}{\omega_{ce} - \omega_l} y_2 + j_p \\ \frac{dy_2}{dt} &= y_1 - i(\omega_l - \omega_{ce}) y_2, \end{aligned} \quad (29)$$

where

$$\begin{aligned} y_0 &= a(s_i, t) , \\ y_1 &= \frac{\partial a(s_i, t)}{\partial t} , \\ y_2 &= e^{-i(\omega_l - \omega_{ce})t} \int_0^t d\tau \frac{\partial a}{\partial \tau} e^{i(\omega_l - \omega_{ce})\tau} . \end{aligned} \quad (30)$$

The first and second order spatial derivatives are given by central difference scheme

$$\begin{aligned} f'(x) &\approx \frac{f(x+h) - f(x-h)}{2h} \\ f''(x) &\approx \frac{f(x+h) - 2f(x) + f(x-h)}{h^2} \end{aligned} \quad (31)$$

The energetic electron current j_p is obtained from the perpendicular velocity moment of energetic particle distribution,

$$j_p(s_i, t) = -\frac{n_{h0}k_l(t)}{4\pi} \iiint \sqrt{2m_e\omega_{ce}(s)(\mathcal{J} + \Omega + \Pi_i)} f e^{i\xi} d\xi d\Omega d\mathcal{J} , \quad (32)$$

where n_{h0} is the density ratio of the energetic electrons to the background cold plasmas. The current integral is solved by interpolating method order by order. The coupled ODEs (29) with respect to time are then solved by the RK method.

To check the contribution of the second order derivatives of slowly vaying kernel $a(s_i, t)$ in the wave equation (28), we further simplify the integral term and obtain the first-order advective wave equation

$$\frac{\partial a}{\partial t} + v_g^l \frac{\partial a}{\partial s_i} = \frac{2\pi v_g^l}{k_l} j_p , \quad (33)$$

where v_g^l is the linear group velocity. For the first-order advective wave equation (33), we apply simple implicit upwind scheme to solve such equation,

$$a_k^{n+1} = \left[S_k^n \pm \frac{\text{imp}}{\Delta s} u_k a_{k\pm 1}^{n+1} + \left(\frac{1}{\Delta t} - \frac{(1 - \text{imp})}{\Delta s} u_k \right) a_k^n \pm \frac{(1 - \text{imp})}{\Delta s} u_k a_{k\pm 1}^n \right] / \left(\frac{1}{\Delta s} + \frac{\text{imp}}{\Delta s} u_k \right) \quad (34)$$

where $u_k = v_g(s = s_k)$, S_k is the source term in the right-hand-side of Eq. (33), **imp** is the combination factor of the implicit-explicit upwind scheme. The sign for the advective term depends on the direction of the group velocity. The absorption boundary condition and fixed noisy initialization condition are applied at the ends of the domain.

As shown in Fig. 6, the first-order wave equation show good approximation to the second-order wave equation and thus the second order term in Eq. (28) may be neglected for the simulation of the onset of chorus wave frequency chirping for computation efficiency.

4. Benchmark Results for the Onset of Rising Tone Chorus

We now conduct several simulations and apply our method to explore the onset of the whistler-mode chorus. We only consider the parallel propagated chorus wave, which is

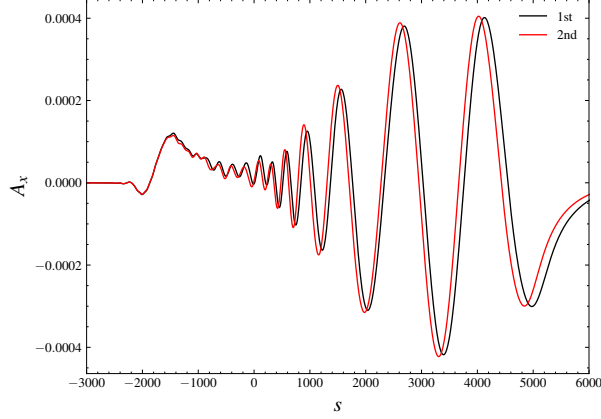


Figure 6: Wave amplitudes calculated from the second-order and first-order wave equations.

consistent with our approximation. The chorus wave has a pure right-handed polarization, thus $a(s_i, t)$ and j_p in Eqs. (28) and (33) can be expressed in a complex scalar, i.e., $a = a_x + ia_y$. The chorus is excited by left propagated resonant electrons, thus the wave propagates toward the right pole along the magnetic field line as a result. The unstable whistler wave is generally arising from the electron temperature anisotropy instability [23, 24], and the growth rate can be obtained from the linear resonance condition near $\Omega \approx 0$,

$$D(\omega_l, k_l; s) = k_l^2(s) - \omega_l^2 - \frac{\omega_p^2(s)\omega_l}{\omega_{ce}(s) - \omega_l} - i2\pi^2 \frac{\omega_{ce}(s)\omega_{h0}^2}{k_l(s)} \int_{-\Pi}^{\infty} dJ(J + \Pi) \frac{\partial f_0}{\partial \Omega} \Big|_{\Omega=0} = 0 \quad (35)$$

In our simulation, the energetic electron distribution is bi-Maxwellian at the magnetic equator. The equilibrium distribution within the i^{th} cell remains the same form as the distribution in the phase space $(s_i, p_{\parallel}, \phi, \varphi)$, i.e.,

$$f_{i0}(\xi, \Omega, \vartheta, J) = \frac{\omega_{ce0}}{(2\pi)^{3/2} v_{th\perp 0}^2 v_{th\parallel 0}} \frac{1}{1 - \beta} \cdot \exp\left(-\frac{k_l^2(\Omega + \Pi_i)^2}{2v_{th\parallel 0}^2}\right) \cdot \left(\exp\left(-\frac{(J + \Omega + \Pi_i)\omega_{ce0}}{v_{th\perp 0}^2}\right) - \exp\left(-\frac{(J + \Omega + \Pi_i)\omega_{ce0}}{\beta v_{th\perp 0}^2}\right) \right), \quad (36)$$

where β is the depth of the loss cone, the subscribe 0 denotes the magnetic equator.

As a realistic model in the magnetosphere, the magnetic field can be approximated as a dipole field, and the major component of the background magnetic field near the equator can be approximatly represented by a parabolic function [25]

$$B(\lambda) = B_0(1 + R_a \lambda^2), \quad (37)$$

where R_a is the inhomogeneity ratio of the magnetic field, B_0 is the magnetic field strength at the equator, and λ is the magnetic latitude. The distance along the magnetic field line s

Table 1: Magnetic field and plasma parameters used in the simulation.

L-shell of the magnetic field line	5
Magnetic field inhomogeneity ratio R_a	4.5
Background cold plasma density inhomogeneity ratio R_b	1.0
Background electro gyro frequency and plasma frequency	$\omega_{ce} = 0.2$ $\omega_{pe} = 1$
Density ratio between energetic and cold electrons at the magnetic equator	0.002
Parallel and perpendicular thermal velocity of energetic electrons	$v_{\perp} = 0.3c$ $v_{\parallel} = 0.15c$
Depth of the loss cone β	0
Size of the simulation domain	$\lambda \in [-15^\circ, 15^\circ]$ $s \in [-6115, 6115]c/\omega_{pe}$

satisfies $s = LR_E\lambda$. The background electron density is found to fit a power law form [26],

$$n(\lambda) = n_0 \cos^{-2R_b}(\lambda) \approx n_0(1 + R_b\lambda^2) \quad (38)$$

where R_b is a fitting parameter in an order of one.

4.1. Simulation configuration

In conventional PIC simulations, the inhomogeneity ratio R_a was often enlarged by one or two order of magnitudes to reduce the simulation cost. While one of the benefits of our numerical scheme is that we can apply the realistic parameters of the Earth dipole field. The basic parameters of our simulation are given in Tab. (4.1) Note that, since we apply the electron plasma frequency ω_{pe0} at the equator for time normalization, the value always be 1 desites the L-shell value, which gyrofrequency is dynamcally changes. The profile of the background parameter is shown in Fig. 7. Meanwhile, we show the most unstable

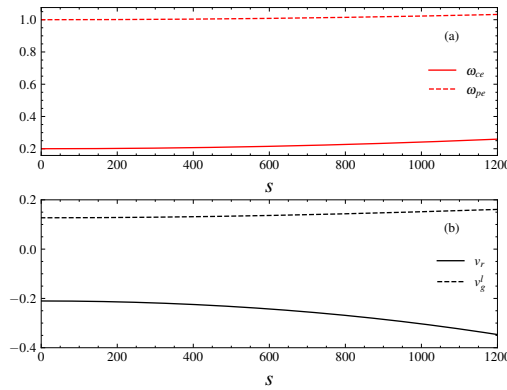


Figure 7: (a) Background magnetic field and density profile. (b) Characteristic velocity in our simulation.

wave frequency applied in the simulation for the determination of initial reference frame.

According to the chosen parameter in Tab. (4.1) and the definition of growth rate γ_l at the equator

$$\gamma_l(s) = \frac{\sqrt{2\pi}\omega_{ce}v_g\omega_{h0}^2}{4k_l^2v_{th||0}} e^{-\frac{(\omega_l-\omega_{ce})^2}{2k_l^2v_{th||0}}} \cdot \left((1+\beta) \frac{T_{\perp 0}}{T_{||0}} \frac{\omega_{ce0}-\omega_l}{\omega_{ce0}} - 1 \right) \quad (39)$$

The most unstable frequency are $\gamma_l \simeq 3.24 \times 10^{-4}$ and $\omega_l = 0.061$. A scan of the parameter is given in Fig. 8.

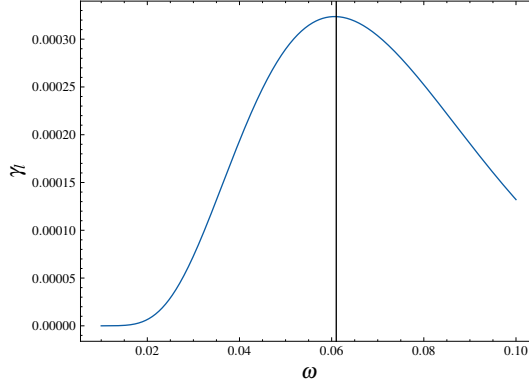


Figure 8: Linear growth rate γ with respect to ω in the chosen parameter. The initial frequency of the wave is obtained from the most unstable frequency indicated by the vertical black line.

5. Benchmarks results

We first present the detailed growth and evolution of the wave, by showing four time snapshots of wave complex components in figure 9. In the beginning of the simulation, the whistler-mode wave is set at noise level, and the energetic electron anisotropy results in the linear whistler wave instability, and cause the exponential growth of the wave amplitude, indicated in Fig. 9(a). While in Fig. 9(b)-(c), after the wave amplitude reached sufficient level, nonlinear resonant trapping occurs, and the chorus wave is initially triggered near the equator by the resonant electrons moving from the right to the left. The wave is propagating in the opposite direction to the resonant particles, chirping and amplifying continuously in this stage.

The linear physics are verified quantitatively in Fig. 10, where we calculate the growth rate and the velocity of the maximum wave amplitude location before the nonlinearity take over. For the propagating wave, we estimate the amplitude growth along its propagation path, the growth rate is given by [27]

$$\Gamma = \frac{1}{t_1 - t_0} \log \frac{|a(s_1, t_1)|}{|a(s_0, t_0)|}, \quad (40)$$

where s_0, t_0, s_1, t_1 are along the prppagation path.

Here we trace the movement of the maximum amplitude point. Its propagation is in accord with the linear group velocity, as shown in Fig. 10(a). The growth of the amplitude

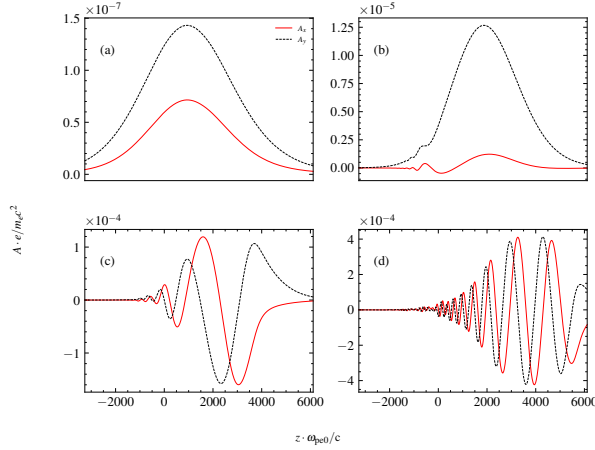


Figure 9: Time snapshots of wave complex amplitude. The red and black curves represent the real and imaginary components of the complex vector potential, respectively. Subplots (a)-(d) indicate the wave amplitude at different time.

along the propagation path is also shown in Fig. 10(b). We calculate the growth rate from equation (40), which is $\Gamma_0 \simeq 3.21 \times 10^{-4}$, agrees well with the theoretic linear growth rate shown in Fig. 8. The results show the correctness of our simulation at linear stage.

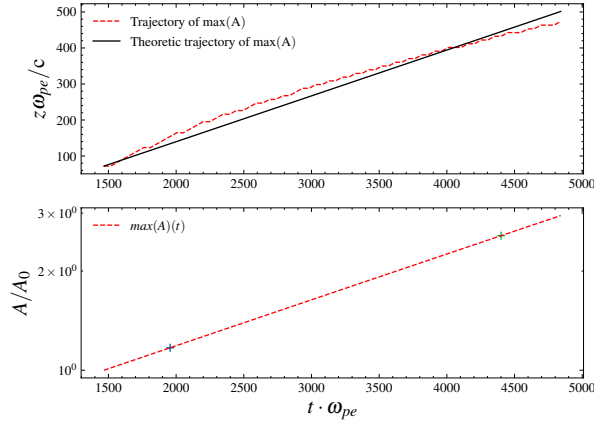


Figure 10: Figure (a) is the propagation velocity of the linear wave packet with the maximum amplitude. Figure (b) denotes the growth of the wave peak amplitude with time along wave propagation path. The green cross marks the point used to calculate the growth rate.

Other than the linear physics seen from Fig. 9(a), we can see that the generation, amplification, and propagation of the nonlinear chorus wave in Fig. 9(b-d). The phase difference between the a_x and a_y components is $\pi/2$ for the nonlinear chorus wave, which is the characteristic of right hand polarized wave. The wave tail becomes more oscillatory, and eventually out of phase near the equator at the end. The reason is that the numerical breakdown of the periodic boundary condition in our simulation. Besides, the most important feature, i.e., the frequency sweeping in this case is shown in figure 11 (a). The frequency of chorus

in our simulation is calculated using the definition of eikonal function, i.e. $\omega = \partial\phi/\partial t$. In addition, we apply empirical mode decomposition (EMD) on the original data to separate the main component and high order frequency oscillation due to finite bandwidth of chorus.

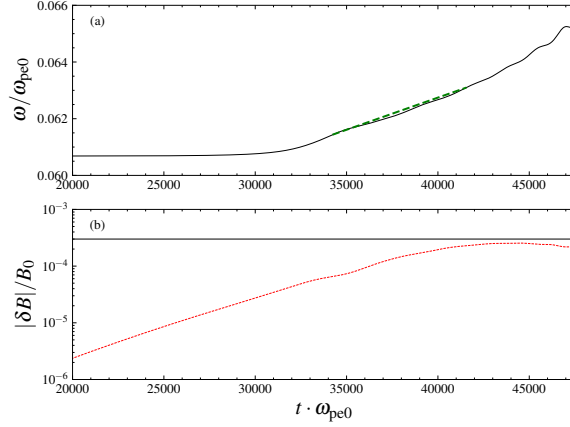


Figure 11: The evolution of the wave frequency and amplitude, where (a) is the frequency chirping and (b) denotes the amplitude growth. The frequency evolution at position $s = 531$ is present. Wave amplitude is given in magnetic field induction $\delta B/B_0$, where B_0 is the background magnetic field at the magnetic equator.

In the liner stage, the wave frequency remains constant, and at around $t = 30000$, wave frequency is increasing from the most unstable frequency $\omega_l = 0.061$, and chirped to around 0.065 in 12500 electron oscillation periods. The corresponding chirping rate is about 2.38 kHz/s, agrees well with the observation. The wave growth shown in Fig. 11 (b) have the same tendency. At the linear stage, the wave is exponential growing, and begin to saturate at nonlinear stage, the saturation level is around $2.5 \times 10^{-4} B_0$, also in well agree with the observation and other numerical simulations.

Our simulation also the dedicated phase-space structure of the resonant particles. In Fig. 12, we show a typical electron phase-space hole at the end stage of the simulation. We also depicted the boundary of the hole from the adiabatic theory, and calculated the size and momentum displacement of the hole, the corresponding $\alpha = 0.08$ and $\omega_b = 0.01125$. The values are well-matched with the theoretic results.

6. Conclusion

In summary, we developed a hybrid-Lagrangian-Eulerian method for the resonance tracking Vlasov system. The method separately solves the perturbed wave particle interaction in fast-varying Hamiltonian subspace, while push the Lagrangian marker in the slowly varying Hamiltonian subspace. We run several simulations for the whistler mode chorus in the Earth magnetosphere for benchmark. The result not only show good agreement with previous results, it also shows high resolution results of the resonant particle phase space. The outcomes of this research promise far-reaching implications across various scientific disciplines, including fusion research, space physics, and astrophysics. A more precise grasp of nonlinear wave-particle interactions in inhomogeneous magnetic fields could pave the way

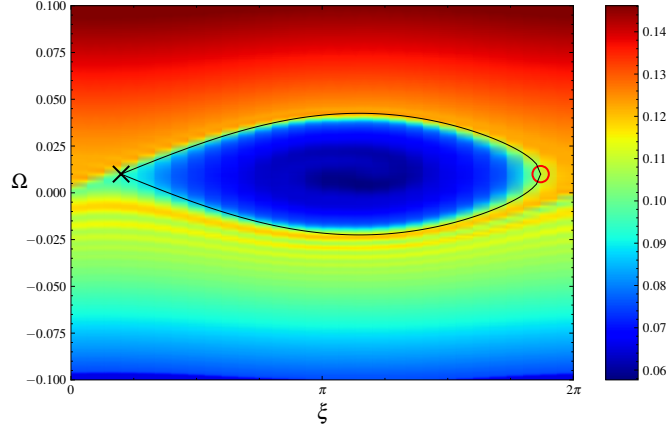


Figure 12: Phase-space hole formed by trapped electrons in the wave field. The size and location of the hole, i.e., the X, C points, and the boundary, are determined from the adiabatic theory.

for enhanced control and manipulation of plasma behavior, enabling advancements in energy generation, propulsion, and space exploration. This paper thus serves as a pivotal stepping stone towards unlocking the untapped potential of nonlinear plasma physics in complex magnetic field environments.

References

- [1] L. Chen, F. Zonca, Physics of Alfvén waves and energetic particles in burning plasmas, *Rev. Mod. Phys.* 88 (2016) 72.
- [2] G. Wang, H. Berk, B. Breizman, L.-J. Zheng, Frequency chirping in the Alfvén continuum, *Nuclear Fusion* 58 (2018) 082014.
- [3] A. Fasoli, C. Gormenzano, H. L. Berk, B. Breizman, S. Briguglio, D. S. Darrow, N. Gorelenkov, W. W. Heidbrink, A. Jaun, S. V. Konovalov, R. Nazikian, J.-M. Noterdaeme, S. Sharapov, K. Shinohara, D. Testa, K. Tobita, Y. Todo, G. Vlad, F. Zonca, Chapter 5: Physics of energetic ions, *Nuclear Fusion* 47 (2007) S264–S284.
- [4] B. T. Tsurutani, E. J. Smith, Postmidnight chorus: A substorm phenomenon, *Journal of Geophysical Research* (1896-1977) 79 (1974) 118–127.
- [5] B. Van Compernelle, X. An, J. Bortnik, R. M. Thorne, P. Pribyl, W. Gekelman, Excitation of Chirping Whistler Waves in a Laboratory Plasma, *Physical Review Letters* 114 (2015) 245002.
- [6] B. Van Compernelle, X. An, J. Bortnik, R. M. Thorne, P. Pribyl, W. Gekelman, Laboratory simulation of magnetospheric chorus wave generation, *Plasma Physics and Controlled Fusion* 59 (2017) 014016.
- [7] S. Kasahara, Y. Miyoshi, S. Yokota, T. Mitani, Y. Kasahara, S. Matsuda, A. Kumamoto, A. Matsuoka, Y. Kazama, H. U. Frey, V. Angelopoulos, S. Kurita, K. Keika, K. Seki, I. Shinohara, Pulsating aurora from electron scattering by chorus waves, *Nature* 554 (2018) 337–340.
- [8] G. D. Reeves, H. E. Spence, M. G. Henderson, S. K. Morley, R. H. W. Friedel, H. O. Funsten, D. N. Baker, S. G. Kanekal, J. B. Blake, J. F. Fennell, S. G. Claudepierre, R. M. Thorne, D. L. Turner, C. A. Kletzing, W. S. Kurth, B. A. Larsen, J. T. Niehof, Electron Acceleration in the Heart of the Van Allen Radiation Belts, *Science* 341 (2013) 991–994.
- [9] R. M. Thorne, W. Li, B. Ni, Q. Ma, J. Bortnik, L. Chen, D. N. Baker, H. E. Spence, G. D. Reeves, M. G. Henderson, C. A. Kletzing, W. S. Kurth, G. B. Hospodarsky, J. B. Blake, J. F. Fennell, S. G. Claudepierre, S. G. Kanekal, Rapid local acceleration of relativistic radiation-belt electrons by magnetospheric chorus, *Nature* 504 (2013) 411–414.

- [10] M. K. Lilley, B. N. Breizman, S. E. Sharapov, Destabilizing Effect of Dynamical Friction on Fast-Particle-Driven Waves in a Near-Threshold Nonlinear Regime, *Physical Review Letters* 102 (2009) 195003.
- [11] B. N. Breizman, Nonlinear travelling waves in energetic particle phase space, *Nuclear Fusion* 50 (2010) 084014.
- [12] H. Hezaveh, Z. Qu, B. Layden, M. Hole, Impact of energetic particle orbits on long range frequency chirping of BGK modes, *Nuclear Fusion* 57 (2017) 126010.
- [13] H. Hezaveh, Z. S. Qu, B. N. Breizman, M. J. Hole, Long range frequency chirping of Alfvén eigenmodes, *Nuclear Fusion* 60 (2020) 056014.
- [14] H. Hezaveh, Z. S. Qu, M. J. Hole, R. L. Dewar, Theoretical description of chirping waves using phase-space waterbags, *Plasma Physics and Controlled Fusion* 63 (2021) 065008.
- [15] C. M. Bender, S. A. Orszag, *Advanced Mathematical Methods for Scientists and Engineers I*, Springer New York, New York, NY, 1999. URL: <http://link.springer.com/10.1007/978-1-4757-3069-2>. doi:10.1007/978-1-4757-3069-2.
- [16] F. Arecchi, R. Bonifacio, Theory of optical maser amplifiers, *IEEE Journal of Quantum Electronics* 1 (1965) 169–178.
- [17] N. Bleistein, R. A. Handelsman, *Asymptotic Expansions of Integrals*, Dover Publications, New York, 1986.
- [18] V. Guillemin, S. Sternberg, *Geometric Asymptotics*, volume 14 of *Mathematical Surveys and Monographs*, revised ed., American Mathematical Society, Providence, Rhode Island, 1977. URL: <http://www.ams.org/surv/014>. doi:10.1090/surv/014.
- [19] T. Shiroto, A. Matsuyama, M. Yagi, A charge-momentum-energy-conserving 1D3V hybrid Lagrangian–Eulerian method for Vlasov–Maxwell system, *Journal of Computational Physics* 469 (2022) 111522.
- [20] K. Imadera, Y. Kishimoto, D. Saito, J. Li, T. Utsumi, A numerical method for solving the Vlasov–Poisson equation based on the conservative IDO scheme, *Journal of Computational Physics* 228 (2009) 8919–8943.
- [21] E. Sonnendrücker, J. Roche, P. Bertrand, A. Ghizzo, The Semi-Lagrangian Method for the Numerical Resolution of the Vlasov Equation, *Journal of Computational Physics* 149 (1999) 201–220.
- [22] G.-H. Cottet, Semi-Lagrangian particle methods for high-dimensional Vlasov–Poisson systems, *Journal of Computational Physics* 365 (2018) 362–375.
- [23] C. F. Kennel, H. E. Petschek, Limit on stably trapped particle fluxes, *Journal of Geophysical Research* 71 (1966) 1–28.
- [24] C. F. Kennel, Velocity Space Diffusion from Weak Plasma Turbulence in a Magnetic Field, *Physics of Fluids* 9 (1966) 2377.
- [25] X. Tao, A numerical study of chorus generation and the related variation of wave intensity using the DAWN code, *Journal of Geophysical Research: Space Physics* 119 (2014) 3362–3372.
- [26] R. E. Denton, Electron density in the magnetosphere, *J. Geophys. Res.* 109 (2004) A09215.
- [27] T. Nogi, Y. Omura, Nonlinear Signatures of VLF-Triggered Emissions: A Simulation Study, *JGR Space Physics* 127 (2022) e2021JA029826.